



## Electrochemical reduction of CO<sub>2</sub> on defect-rich Bi derived from Bi<sub>2</sub>S<sub>3</sub> with enhanced formate selectivity

Ying Zhang,<sup>a,b</sup> Fengwang Li,<sup>a,b</sup> Xiaolong Zhang,<sup>a</sup> Tim Williams,<sup>c</sup> Christopher D. Easton,<sup>d</sup> Alan. M. Bond<sup>\*a,b</sup> and Jie Zhang<sup>\*a,b</sup>

Received 00th January 20xx,  
Accepted 00th January 20xx

DOI: 10.1039/x0xx00000x

[www.rsc.org/](http://www.rsc.org/)

A sulphide-derived bismuth catalyst, synthesised from a one-pot hydrothermal reaction followed by electrochemical reduction, exhibits excellent performance for converting CO<sub>2</sub> into formate in an aqueous bicarbonate medium with high activity, selectivity and durability. The maximum faradaic efficiency for formate formation of 84.0 % was achieved at an overpotential of 670 mV. Detailed study reveals that the lattice defects associated with the sulphide-derived derived Bi rather than residual sulphur are likely to engender a positive effect on the catalytic reduction of CO<sub>2</sub>.

### 1. Introduction

The electrochemical reduction of carbon dioxide (CO<sub>2</sub>) using electricity generated from intermittent renewable sources is a promising approach for recycling CO<sub>2</sub> with significant economic and environmental benefit.<sup>1</sup> To realize this dream, different materials and optimization strategies have been explored to develop an optimal electrochemical CO<sub>2</sub> reduction strategy. However, the vast array of approaches and still immature understanding of the reaction mechanisms make it challenging to assess the maximum potential.<sup>2</sup> Especially, it is now widely recognized that catalysts, which exhibit high CO<sub>2</sub> reduction selectivity and low overpotential, and the ability to inhibit the competing hydrogen evolution reaction, are crucially needed.

d- (e.g. Cu, Pd, Ag, Au) and p-block metals (e.g. Pb, In, Sn, Bi) are frequently used as electrocatalysts for CO<sub>2</sub> reduction to produce CO, formate, oxygenates and hydrocarbons in aqueous electrolyte media<sup>3-5</sup> via mechanisms that involve the formation of an adsorbed CO<sub>2</sub><sup>-</sup> anion radical species followed by catalyst dependent steps.<sup>6</sup> Usually, polycrystalline metal foils display a poor product selectivity and efficiency unless a large overpotential is applied.<sup>7</sup> Strategies involving nanostructuring, alloying, doping and multiphasing have been developed to boost the activity of these metal catalysts.<sup>8-13</sup> In principle, another strategy is to create high energy intrinsic lattice defects, such as dislocations, stepped surfaces and boundaries.

Even though this concept has been widely explored in water splitting reactions,<sup>14</sup> only limited research works have been undertaken to explore the application of this strategy on the far more complicated CO<sub>2</sub> reduction reaction. Introduction of defects can increase the number of active sites available for electrochemical reactions. For example, Kanan and co-workers reported that grain boundaries could engender high activity for CO<sub>2</sub> reduction using Au and Cu nanoparticles supported on carbon nanotubes (CNT).<sup>15, 16</sup> They found a strong correlation between grain boundary surface density and catalytic activity, which suggests that grain boundaries alter the surface properties and lower the barrier for CO<sub>2</sub> reduction reaction. Grain boundary-rich Au/CNT and Cu/CNT were found to have best selectivity.

In an early study, Frese reported that intentionally oxidized copper electrodes could improve the faradaic efficiency of methanol formation due to the presence of Cu<sub>2</sub>O but with a lower current density since the conductivity of Cu<sub>2</sub>O is not ideal<sup>17</sup>. Recently, as a representative strategy to create defect-rich catalysts, many oxide-derived materials have been introduced for catalysing the electrochemical CO<sub>2</sub> reduction. Kanan and co-workers pointed out that reducible metal composites based on oxide-derived Au, oxide-derived Cu and Sn/SnO<sub>x</sub> thin films have remarkable catalytic properties for CO<sub>2</sub> conversion.<sup>18-20</sup> These oxide-derived electrocatalysts possess a higher level of surface defects/residual oxygen, resulting in enhanced CO<sub>2</sub> reduction capabilities. Based on a similar idea, our group has synthesized sulphide and sulphide-derived metals,<sup>21-23</sup> such as Sn/SnS<sub>2</sub> derived from SnS<sub>2</sub> nanosheet supported on reduced graphene oxide, which display superior catalytic activity in aqueous electrolyte solutions compared to their pure metallic counterparts.<sup>23</sup> Sulphides are a common class of minerals found in Nature, and many sulphides have higher conductivity than oxides which enhances the kinetics of electron transfer and hence catalytic activity.<sup>24</sup> In principle, sulphide-derived materials should have similar defects as those

<sup>a</sup>School of Chemistry, Monash University, Wellington Road, Clayton 3800, VIC, Australia. E-mail: Alan.Bond@monash.edu and Jie.Zhang@monash.edu

<sup>b</sup>ARC Centre of Excellence for Electromaterials Science, Monash University, Wellington Road, Clayton 3800, VIC, Australia

<sup>c</sup>Monash Centre for Electron Microscopy, Monash University, Clayton 3800, Victoria, Australia

<sup>d</sup>CSIRO Manufacturing, Bayview Ave, Clayton 3168, Victoria, Australia

<sup>†</sup>Electronic Supplementary Information (ESI) available: The details for characterization of materials including XPS, XRD, SEM and TEM. Electrochemical measurement data including cyclic voltammograms and detailed bulk electrolysis results. See DOI: 10.1039/x0xx00000x

created in the oxide-derived materials. Furthermore, the residual sulphur (correspondingly, oxygen in oxide-derived materials<sup>25, 26</sup>) may also alter the adsorption properties of CO<sub>2</sub> and its reduction intermediates and therefore tune the activity and selectivity of the CO<sub>2</sub> reduction reaction, similar to the effect of halides recently reported by Gao et al.<sup>27</sup> The sulphide-derive strategy has been gradually recognised and applied by the research community as an effective approach to optimise the CO<sub>2</sub> reduction performance of Cu and Sn.<sup>22, 23, 28, 29</sup> For example, sulphur dopants have been found to contribute to the enhanced catalytic selectivity of Cu towards formate.<sup>28</sup> Despite these emerging progresses in sulphide-derived materials, the understanding of the intrinsic and surface structure of these materials is limited.

Bi, as a non-toxic and inexpensive electrocatalyst, has attracted a great deal of scientific interest for CO<sub>2</sub> reduction because it can achieve a relatively high faradaic efficiency towards formate formation in aqueous electrolyte media<sup>30, 31</sup> and CO formation in organic electrolyte media<sup>32, 33</sup> at a moderate overpotential. So far, the morphology effect (nanostructuring strategy) of Bi-based catalysts has been well studied while the true active site of the catalytic reaction of these catalysts has rarely been discussed. Therefore, in this work, we introduce an excellent defect-rich Bi electrocatalyst for CO<sub>2</sub> reduction, derived from reduction of Bi<sub>2</sub>S<sub>3</sub> in a CO<sub>2</sub> saturated aqueous bicarbonate solution. A maximum of 84.0 % faradaic efficiency is achieved for generation of formate with only a negligible loss of faradaic efficiency in a 24 h durability test. Evidenced by microscopic characterisations, a lattice disordering defect-rich Bi derived from Bi<sub>2</sub>S<sub>3</sub> rather than residual sulphur is the key factor contributing to the high formate selectivity in the electrochemical reduction of CO<sub>2</sub>.

## 2. Experimental Section

### 2.1. Chemicals

Bismuth nitrate pentahydrate (≥99.99%), thiourea (≥99.0%), deuterium oxide (99.9 atom % D) and nafion (5 wt%) were purchased from Sigma-Aldrich; sodium bicarbonate (ACS grade), ethanol (99.7%), acetone (≥ 99.0%) and dimethylsulfoxide (99.9%) were purchased from Merck; nitrogen (99.999%) and carbon dioxide (> 99.9%, Aligal) were purchased from Air Liquide, Australia; bismuth foil (99.9%) was purchased from Zr-industrial, Shanghai, China. Except for bismuth foil, which was abraded with sand paper prior to experiments, all other chemicals were used as supplied. All aqueous solutions were prepared using high purity water obtained from a Milli-Q water (18.2 MΩ cm) purification system.

### 2.2. Synthesis of Bi<sub>2</sub>S<sub>3</sub>

Bismuth sulphide was synthesized by a method adapted from a previous report.<sup>34</sup> Typically, 30 mg of bismuth nitrate pentahydrate and 70 mg of thiourea were dissolved in 18 ml water. Next, the solution was transferred into a 20 ml Teflon-

lined autoclave and heated at 200 °C for 24 h. After cooling to room temperature, the black precipitate was collected by centrifugation and washed with water three times. Finally, the black sample was dried under vacuum.

### 2.3. Preparation of sulphide derived-Bi (SD-Bi) electrodes

Typically, 4 mg of as-prepared Bi<sub>2</sub>S<sub>3</sub> sample was dispersed in 1 ml water and sonicated to form a homogeneous solution. Next, 6 μl dispersion solution was pipetted onto a 3 mm diameter glassy carbon electrode (geometric area is 0.0707 cm<sup>2</sup>). The SD-Bi electrode was prepared by electrochemical reduction for 30 mins at an applied potential of -0.75 V vs. RHE in CO<sub>2</sub> saturated 0.5 M NaHCO<sub>3</sub> solutions, and evaluated by CO<sub>2</sub> reduction bulk electrolysis and cyclic voltammetric measurements in the same solution. The electrode used for bulk electrolysis was fabricated using a 1 cm × 1.5 cm glassy carbon plate as the substrate with corresponding amount of Bi<sub>2</sub>S<sub>3</sub> samples. 5% v/v nafion was added to prepare the electrode for long time bulk electrolysis test for 24 hours, while the rest electrodes for electrolysis were prepared without nafion since the adhesion of fresh prepared SD-Bi is good on the measurement timescale.

### 2.4. Preparation of Bi foil electrodes

Prior to experiments, the Bi foil electrode was polished with fine sand paper and then washed with water and ethanol, and finally dried under a stream of N<sub>2</sub>. The Bi foil electrode used for cyclic voltammetric experiments had a geometric area of 0.24 cm<sup>2</sup> while the one used for bulk electrolysis had a geometric area of 1.5 cm<sup>2</sup>.

### 2.5. Annealing of SD-Bi electrodes

After rinsing with water and drying under a stream of N<sub>2</sub>, the SD-Bi electrode was placed in a tube furnace under an N<sub>2</sub> atmosphere at 150 °C for 2 h. The electrode was then analysed by TEM and used for CO<sub>2</sub> reduction under bulk electrolysis conditions.

### 2.6. Electrochemical characterization

Cyclic voltammetric (CV) measurements were undertaken with a CHI 760E electrochemical workstation. A standard three-electrode setup was used with the SD-Bi electrode as the working electrode together with the Ag/AgCl (1 M KCl) as reference electrode and platinum wire as counter electrode. All electrochemical experiments were undertaken at room temperature (22 ± 2 °C). Bulk electrolysis experiments were undertaken in gas-tight H-shaped electrolysis cell using the modified electrodes as the working electrode, Ag/AgCl (1 M KCl) placed in the same compartment as the reference electrode, and a graphite rod placed in a separated compartment as the counter electrode. The electrolysis cell compartments were separated by a glass frit. Each compartment contained 10 mL of 0.5 M electrolyte solutions (NaHCO<sub>3</sub>). The volume of the headspace was 20 mL. Before bulk electrolysis, the solutions in both compartments were bubbled with CO<sub>2</sub> for at least 30 mins. The formula used to convert potentials vs. Ag/AgCl (1 M) to vs. RHE is:  $E \text{ vs. RHE} = E \text{ (V) vs. Ag/AgCl (1 M KCl)} + 0.222 \text{ (V)} + 0.0586 \text{ (V)} \times \text{pH (22 °C)}$ .

### 2.7. Analysis of the bulk electrolysis products

The gaseous product(s) was collected in a gas-tight syringe (200  $\mu\text{L}$ ) and then analysed by an Agilent (7820 A) gas chromatography system equipped with a HP-plot molesieve (5 $\text{\AA}$ ) column and a thermal conductivity detector (TCD). Specifically,  $\text{H}_2$  was detected using a 24 m length column with  $\text{N}_2$  as the carrier gas while  $\text{CO}$  was detected with a 4 m length column with He as the carrier gas. The liquid product(s) was analysed by  $^1\text{H}$  NMR spectroscopy using a Bruker DRX400 spectrometer at a frequency of 400.2 MHz. NMR samples were prepared by mixing 0.5 mL of the product-containing electrolyte solution with 0.1 mL  $\text{D}_2\text{O}$  solution which contained 100 ppm (v/v) DMSO as the internal standard.

### 2.8. Physical characterization

X-ray diffraction (XRD) data were collected with a Bruker D8 ADVANCED power diffractometer using  $\text{Cu K}\alpha$  radiation ( $\lambda = 0.15406$  nm). X-ray photoelectron spectra (XPS) were recorded using an AXIS Ultra DLD spectrometer (Kratos Analytical, Manchester, UK). A monochromated Al  $\text{K}\alpha$  radiation source was used in these experiments with a power of 180 W (15 kV  $\times$  12 mA) along with a hemispherical analyser operating in the fixed analyser transmission mode and a 110  $\mu\text{m}$  aperture. Survey spectra were acquired at a pass energy of 160 eV while the higher resolution spectra were recorded from individual peaks at 80 eV and 40 eV pass energy. XPS data processing was performed with CaseXPS software version 2.3.15 (Casa Software Ltd., Teignmouth, UK). Scanning electron microscopic (SEM) images were obtained with a FEI Nova NanoSEM 450 FEG SEM Instrument. Transmission electron microscopy (TEM) images and diffraction patterns were acquired with a FEI Tecnai G<sup>2</sup> T20 TWIN TEM operated at 200 kV. Diffraction patterns from different Bi samples were obtained in the TEM diffraction mode using a spot size of 3 or 4. High-angle annular dark-field scanning transmission electron microscopy (HAADF-STEM) images, energy-dispersive X-ray spectra (EDX) and maps were acquired with a FEI Tecnai G2 F20 S-TWIN FEGTEM operated at 200 kV.

## 3. Results and Discussion

### 3.1. Morphology and structure of $\text{Bi}_2\text{S}_3$ and SD-Bi

The procedure for synthesis of  $\text{Bi}_2\text{S}_3$  derived Bi (SD-Bi) is schematically described in Figure 1a. Firstly, urchin-like  $\text{Bi}_2\text{S}_3$  was synthesised through a surfactant-free hydrothermal reaction adapted from a literature report.<sup>34</sup> Then, SD-Bi was obtained through electrochemical reduction. These details, together with the electrode fabrication process, are given in the experimental section. Figures 1b and 1c show the scanning electron microscopy (SEM) images of  $\text{Bi}_2\text{S}_3$  and SD-Bi at low and high (inset) magnifications. Because of relatively high reaction pressure, the homogeneous  $\text{Bi}_2\text{S}_3$  with a micro-urchin structure was self-assembled to give micro-rods with a length of 500-700 nm and a width of 20-50 nm. After electrochemical reduction, the overall morphology in a micro scale remained unaltered.

The crystal structures of  $\text{Bi}_2\text{S}_3$  and SD-Bi were further investigated by examination of x-ray diffraction (XRD) patterns as shown in Figures 1d and 1e and the crystalline phase identified by comparison with diffraction peaks of  $\text{Bi}_2\text{S}_3$  (JCPDS 89-8963) and Bi (JCPDS 44-1246), which have been indexed to orthorhombic  $\text{Bi}_2\text{S}_3$  phase and rhombohedral Bi phase, respectively. Based on the XRD pattern, SD-Bi is composed of pure bismuth only with no  $\text{Bi}_2\text{S}_3$  or  $\text{Bi}_2\text{O}_3$  being detected.

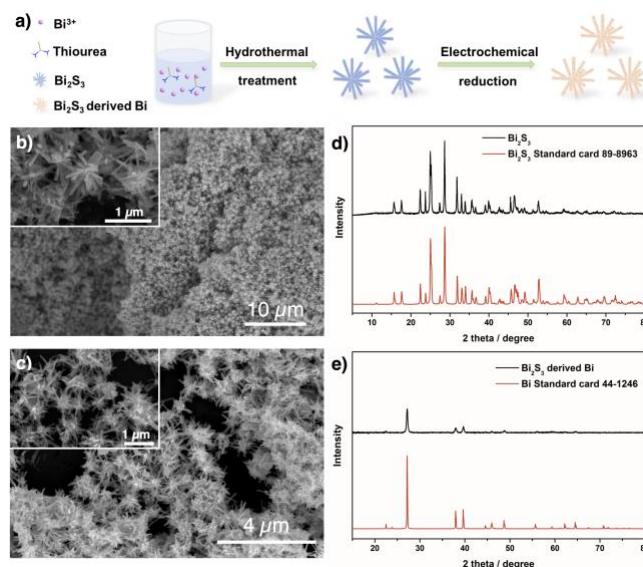


**Figure 1.** (a) Scheme used for the synthesis of  $\text{Bi}_2\text{S}_3$  derived Bi. (b, c) SEM images of  $\text{Bi}_2\text{S}_3$  and SD-Bi respectively at low and high (inset) magnification. (d, e) XRD patterns of  $\text{Bi}_2\text{S}_3$  and SD-Bi (black trace) with corresponding standard patterns (red trace) presented.

Further insights into the morphology and composition of SD-Bi were gained from transmission electron microscopy (TEM), high-angle annular dark-field scanning TEM (HAADF-STEM) and energy-dispersive x-ray (EDX) spectroscopy. TEM and HAADF images revealed that the SD-Bi contained a large number of approximately 5 nm diameter pores in each rod-like branch compared to the original  $\text{Bi}_2\text{S}_3$  which has smooth structure (Figures 2a and 2b). These results indicate that the porous structure was formed during the electrochemical reduction process. This nanoscale morphology transition is attributed to the gradual removal of sulphide from  $\text{Bi}_2\text{S}_3$  upon electrochemical reduction of bismuth. The EDX mapping (Figures 2c and 2d) and spectra (Figure 2e) revealed that the sulphide has been completely reduced to metallic Bi evidenced by the absence of sulphur peaks, which is consistent with the XRD results. Since the residual sulphur if present may also have significant impact on the performance of sulphur derived catalysts as discussed in the Introduction Section, the typical x-ray photoelectron spectra (XPS) survey spectrum and the high-resolution scan of S 2s (Figure S1) were conducted to provide a more precise analysis of the surface chemical composition of the SD-Bi and confirm that no detectable S element exists in the surface of the SD-Bi. A small oxygen signal was detected using both EDX mapping and XPS analysis, which is most likely due to

the exposure of the sample to air, since oxide is only found in the outer layer of SD-Bi as shown in Figure 1d and also noting that  $\text{Bi}_2\text{O}_3$  is thermodynamically unstable under the negative potential of  $-0.75$  V vs. RHE used in this study as discussed in Figure S2 (all potentials hereafter are given with respect to RHE unless otherwise stated).

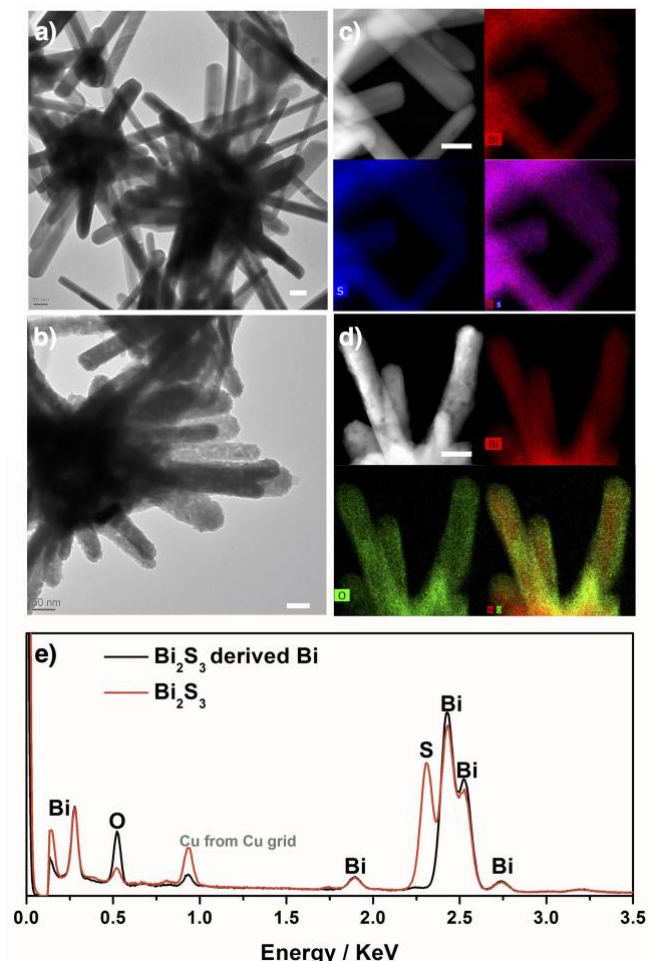


**Figure 2.** TEM, HAADF-STEM images and corresponding EDX mapping results for (a, c)  $\text{Bi}_2\text{S}_3$  and (b, d)  $\text{Bi}_2\text{S}_3$  derived Bi. (e) EDX spectra of  $\text{Bi}_2\text{S}_3$  derived Bi (black line) and  $\text{Bi}_2\text{S}_3$  (red line).

### 3.2. Voltammetric measurements and $\text{CO}_2$ reductive bulk electrolysis with SD-Bi

Cyclic voltammetric (CV) measurements were carried out at a scan rate of  $50 \text{ mV s}^{-1}$  in  $\text{CO}_2$  and  $\text{N}_2$  saturated  $0.5 \text{ M NaHCO}_3$  aqueous solution using a  $\text{Bi}_2\text{S}_3$  modified electrode. As shown in Figure S3a, the reduction of  $\text{Bi}_2\text{S}_3$  occurred in the first negative potential scan as evidenced by a broad process around  $-0.85$  V under stirred condition (same conditions as for bulk electrolysis). This process attributed to the reduction of  $\text{Bi}_2\text{S}_3$  to Bi. The companion oxidation peaks in the reverse cycle can be attributed to the conversion of metallic Bi to  $\text{Bi}_2\text{O}_3$  in a stepwise manner, based on the literature reports.<sup>35-37</sup> In the repetitive cycle of potential, a new reduction peak was observed with a peak potential of  $-0.25$  V due to the reduction of  $\text{Bi}_2\text{O}_3$  to Bi in a single unresolved process.<sup>38</sup> The reduction process associated

with  $\text{Bi}_2\text{S}_3$  almost disappeared completely. Same processes were observed in the 3<sup>rd</sup> and following cycles of potentials. Similar processes were observed in a  $\text{CO}_2$  saturated  $0.5 \text{ M NaHCO}_3$  aqueous solution (Figure S3b). The voltammograms of this SD-Bi modified electrode are shown in Figure 3a. A pre-cleaned Bi foil electrode (see Experimental Section) also was tested with the same conditions but in a fresh  $0.5 \text{ M NaHCO}_3$  aqueous solution for comparison (Figure 3b). The disappearance of  $\text{Bi}_2\text{S}_3$  reduction process and the similarity between the voltammograms obtained with the SD-Bi modified electrode and Bi foil electrode confirm that  $\text{Bi}_2\text{S}_3$  was irreversibly reduced to Bi with  $\text{S}^{2-}$  diffusing into bulk solution.

Significant differences in  $\text{CO}_2$  reduction activity between SD-Bi and Bi foil electrodes were observed when comparing the CV responses (Figure 3a). Both SD-Bi and Bi foil electrodes generate  $\text{CO}_2$  reduction current with similar onset potentials for  $\text{CO}_2$  reduction (around  $-0.55$  V), but the current density based on the substrate geometric area for SD-Bi is about two times higher than that of Bi foil benefiting from its sub-micro to nano structure and certain porosity as shown in Figure 2. A likely reason is that the actual electroactive surface area for nanostructured SD-Bi is larger than that for flat Bi foil. To confirm this hypothesis, the double-layer capacitances were estimated from CV data obtained as a function of scan rates in order to evaluate the electrochemical surface area of the SD-Bi and Bi foil electrodes (Figure S4). The SD-Bi electrode exhibits a significantly larger double layer capacitance ( $0.2278 \text{ mF cm}^{-2}$ ; the contribution of uncover GC electrode to this value is negligible since the capacitance of the bare GC electrode was determined to be  $0.0252 \text{ mF cm}^{-2}$ , as shown in Figure S5) than Bi foil electrode ( $0.0216 \text{ mF cm}^{-2}$ ), which indicates that the SD-Bi electrode has a roughness factor about 10 times higher than the Bi foil electrode, resulting in a far larger electroactive surface area. Even though the geometric current density did not increase 10 times due to the mass transport limitation resulting from the nanoporous structure associated with SD-Bi and low  $\text{CO}_2$  solubility in aqueous electrolyte media under ambient conditions, this is still a relatively high geometric current density found so far from Bi based catalysts.<sup>30, 39</sup>

Bulk electrolysis was conducted to provide conclusive evidence of enhanced  $\text{CO}_2$  reduction activity. Potentials in the range of  $-0.65$  V to  $-1.05$  V using  $0.5 \text{ M CO}_2$  saturated  $\text{NaHCO}_3$  aqueous solution was applied to both electrodes and the faradaic efficiency (FE) of formate was plotted as a function of the applied potential as shown in Figure 3b. The fact that the FE value is significantly less than 100% suggests that other reduction products are present, which were found to be CO and  $\text{H}_2$ . The potential dependent distributions of these two products are shown in Table S1. These results reveal that formate is the dominant product and that the selectivity is strongly dependent on both the applied potential and catalytic activity of the electrode. At an applied potential of  $-0.75$  V (corresponding to an overpotential of  $0.67$  V for formate), formate was generated with its maximum FE of 84.0 % using the SD-Bi electrode while only 49.5 % formate was detected with the Bi foil electrode at

the same applied potential. SD-Bi gives high FE for formate over a broad range of potential from -0.65 V to -1.05 V suggesting that it is highly selective towards formate. The large difference in the FE for formate generation suggests that their intrinsic differences play a significant role in determining the activity with respect to electrochemical CO<sub>2</sub> reduction. Besides, during bulk electrolysis at different potential conditions, the overall morphology of SD-Bi remains same as shown in Figure S6.

### 3.3. Origins of the activity of SD-Bi for electrochemical CO<sub>2</sub> reduction

To explore the intrinsic structure evolution that takes place during electrochemical reduction of Bi<sub>2</sub>S<sub>3</sub>, high resolution TEM (HRTEM) images were collected. Figure 4a shows HRTEM images of the well-defined Bi<sub>2</sub>S<sub>3</sub> before electrolysis, which displays high crystallinity with well-defined lattice fringes. The interplanar spacing of the lattice fringe is 0.79 nm corresponding to the (110) plane of Bi<sub>2</sub>S<sub>3</sub>. In contrast, SD-Bi does not show clear lattice fringes at the same magnification (Figure 4b). Under the higher magnification conditions used in Figure 4c, crystalline features with a lattice fringe of 0.22 nm corresponding to the (110) plane of crystalline Bi as well as localised disordered (glassy) atomic-scale structures of Bi were both observed. The selected area electron diffraction (SAED) patterns insets to Figures 4a and 4b provides additional information on the degree of crystallinity of the two samples, which were taken from a group of Bi<sub>2</sub>S<sub>3</sub> and SD-Bi crystals. The rings of clear spots were observed for Bi<sub>2</sub>S<sub>3</sub> shown in inset of Figure 4a, whereas the SAED pattern of SD-Bi is more or less continuous rings (inset, Figure 4b), indicating only nanocrystallinity.

The origin of the structural transformation is the release of lattice sulphur during electrochemical CO<sub>2</sub> reduction, which induces a structural disorder to the catalyst. When applying a negative electrode potential, the fast releasing of S<sup>2-</sup> upon Bi<sup>3+</sup> reduction to Bi creates surface vacancies that initiates structural rearrangement leading to the formation of nano-scale porosity and atomic-scale disordering in the reaction zone.

Further experiments were conducted to confirm the importance of structural disorder towards electrochemical CO<sub>2</sub> reduction activity. Since the structural disorder (between polycrystalline and amorphous phase) can be crystallised completely into an ultrafine polycrystalline material through controlling the crystallisation kinetics (heat treatment conditions),<sup>40</sup> the SD-Bi electrode was annealed for 30 min at 150 °C under a N<sub>2</sub> atmosphere prior to being used in bulk electrolysis to increase its crystallinity and decrease surface defects. After annealing, while the morphology remains unaltered as shown in Figure S7, the crystallinity increases as suggested by the SAED pattern (Figure S7a) and the HRTEM image (Figure S7c). The former shows clear diffraction spots instead of continuous rings observed from the same sample before annealing (Figure 4b). The XRD results (Figure S8) consistently indicate an enhanced intensity of all the deflection peaks after annealing SD-Bi due to improved crystallinity. To make a fair comparison, same instrumental parameters and sample quantities were used.<sup>41</sup> Besides, the decrease of peak width at half high also confirm that a more ordered and better crystalline structure was formed after annealing. For comparison, the XRD pattern of Bi foil was shown in Figure S9. The sharp and intense peaks indicate that Bi foil has a highly crystalline metallic phase. The annealed SD-Bi electrode exhibited a low FE for formate but a similar total current density to that displayed by an annealed SD-Bi electrode as shown in Figure 5, which indicates that surface defects induced lattice disordering is a significant factor in CO<sub>2</sub> reduction activity. This observation is consistent with that found from oxide-derived catalytic materials.<sup>18</sup> In this study, the larger atomic radius of sulphur facilitates the formation of defect-rich Bi. This observation also concludes (based on the comparison of FE values obtained from SD-Bi, annealed SD-Bi and Bi foil) that microstructure of SD-Bi does not contribute significantly to its formate selectivity but contributes to the increase of geometric current density.

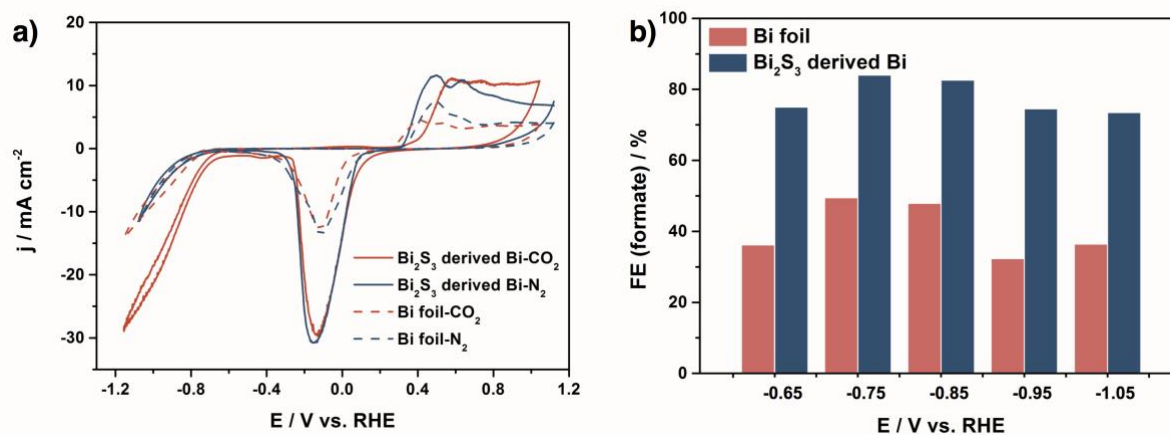


**Figure 3.** (a) Cyclic voltammograms obtained with a scan rate of 50 mV s<sup>-1</sup> in CO<sub>2</sub> and N<sub>2</sub> saturated 0.5 M NaHCO<sub>3</sub> aqueous solution using SD-Bi and Bi foil electrodes. (b) Comparison of faradaic efficiency of formate production on SD-Bi and Bi electrodes at designed potentials using a CO<sub>2</sub> saturated 0.5 M NaHCO<sub>3</sub> aqueous solution.

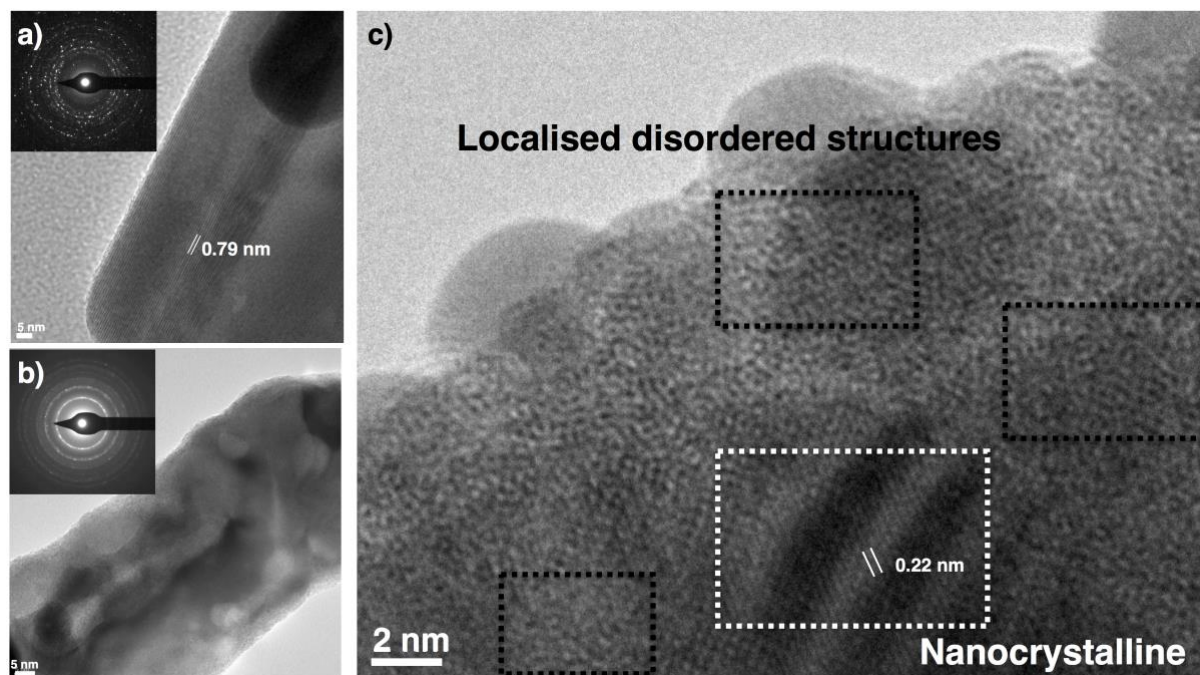


**Figure 4.** HRTEM images of (a)  $\text{Bi}_2\text{S}_3$  and (b, c) SD-Bi. The white square indicates the presence of well crystallised metallic Bi while the black square is indicative of the localised disordered structures of Bi. Insets of (a, b) are the SAED patterns.

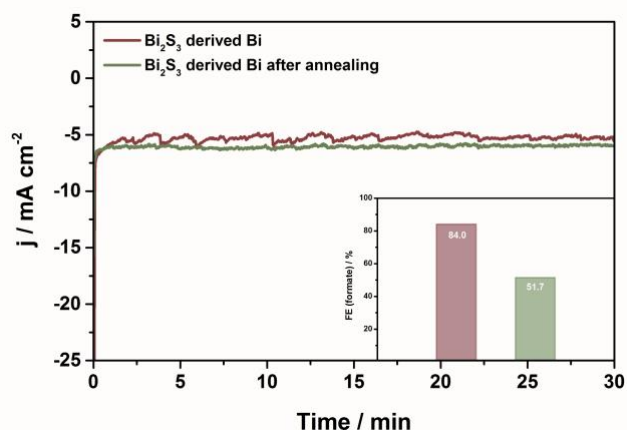


**Figure 5.** Total current density vs. time for electrolysis at  $-0.75$  V using (a) SD-Bi electrode and (b) SD-Bi electrode post annealing at  $150$  °C for 30 min. Bottom-right inset is the final faradaic efficiency of formate measured after electrolysis.

### 3.4. Long-term stability of SD-Bi

To evaluate the durability of the SD-Bi electrode, a long-term electrolysis experiment was conducted with an applied potential of  $-0.75$  V over 24 h (Figure 6). During electrolysis, the current density was stable at about  $5 \text{ mA cm}^{-2}$  and the FE for formate remained essentially unchanged. The morphology and porous structure did not change over the 24 h electrolysis duration (Figure S6 and S10) and HETEM confirmed that the surface defects remained as shown in Figure S10c.

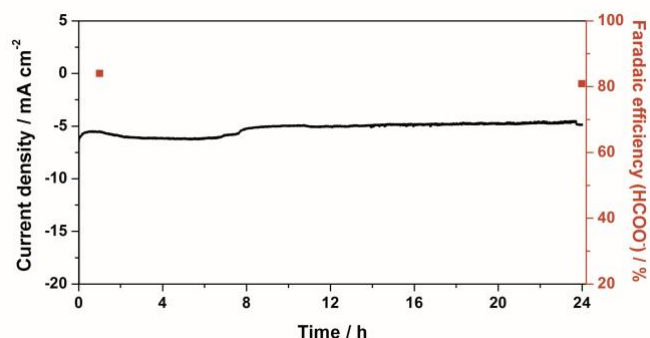


**Figure 6.** Time dependence of current density and faradaic efficiency for formate production using a SD-Bi electrode at a potential of  $-0.75$  V in  $\text{CO}_2$  saturated  $0.5 \text{ M NaHCO}_3$  solutions over a 24 h period.

## 4. Conclusions

In summary, we have synthesised a SD-Bi catalyst via a hydrothermal reaction followed by electrochemical reduction to induce a defect-rich Bi structure. Microscopic evidence combined with electrochemical measurements show that the surface defects induced lattice disordering structure rather than residual sulphur accelerates the catalysis of  $\text{CO}_2$  reduction to formate. This heterogeneous catalyst has high activity, selectivity and durability for converting  $\text{CO}_2$  into formate in aqueous bicarbonate medium. The maximum faradaic efficiency achieved for generation of formate is  $84.0\%$  at a relatively low potential of  $-0.75$  V and remains unchanged over 24 h. More broadly, this work gives insights into how the

performance of sulphide-derived metal for CO<sub>2</sub> reduction reaction may be optimised and opens up new possibilities for developing highly active and stable catalysts based on reducible metal composites. Even though the selectivity of Bi derived from Bi<sub>2</sub>S<sub>3</sub> is excellent, further increase in the current density is needed to surpass the threshold for commercial applications.

### Conflicts of interest

There are no conflicts to declare.

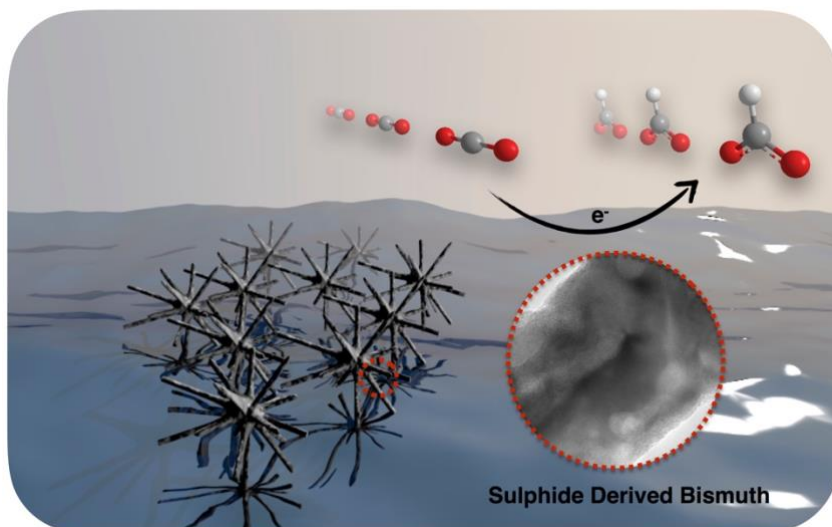
### Acknowledgements

This work was supported by the Australian Research Council (ARC) through the ARC Centre of Excellence for Electromaterials Science and a Discovery Project. YZ is grateful to the Science Faculty at Monash University for the award of a Dean's Postgraduate Research Scholarship and the China Scholarship Council for a scholarship enable the studies described in this paper to be undertaken at Monash University. The authors acknowledge the use of facilities in the Monash Centre for Electron Microscopy (funded by ARC grant LE110100223) and the Monash X-Ray Platform.

### Notes and references

- V. Quaschnig, *Understanding renewable energy systems*, Routledge, 2016.
- G. O. Larrazábal, A. J. Martín and J. Pérez-Ramírez, *J. Phys. Chem. Lett.*, 2017, **8**, 3933-3944.
- Q. Lu and F. Jiao, *Nano Energy*, 2016, **29**, 439-456.
- C. Cao and Z. Wen, *J. CO<sub>2</sub> Util.*, 2017, **22**, 231-237.
- P. Huang, S. Ci, G. Wang, J. Jia, J. Xu and Z. Wen, *J. CO<sub>2</sub> Util.*, 2017, **20**, 27-33.
- D. D. Zhu, J. L. Liu and S. Z. Qiao, *Adv. Mater.*, 2016, **28**, 3423-3452.
- Y. Hori, H. Wakebe, T. Tsukamoto and O. Koga, *Electrochim. Acta*, 1994, **39**, 1833-1839.
- D. Gao, H. Zhou, J. Wang, S. Miao, F. Yang, G. Wang, J. Wang and X. Bao, *J. Am. Chem. Soc.*, 2015, **137**, 4288-4291.
- S. Rasul, D. H. Anjum, A. Jedidi, Y. Minenkov, L. Cavallo and K. Takanebe, *Angew. Chem.*, 2015, **127**, 2174-2178.
- K. Nakata, T. Ozaki, C. Terashima, A. Fujishima and Y. Einaga, *Angew. Chem. Int. Ed.*, 2014, **53**, 871-874.
- P. P. Sharma, J. Wu, R. M. Yadav, M. Liu, C. J. Wright, C. S. Tiwary, B. I. Yakobson, J. Lou, P. M. Ajayan and X. D. Zhou, *Angew. Chem. Int. Ed.*, 2015, **54**, 13701-13705.
- S.-F. Zhao, M. Horne, A. M. Bond and J. Zhang, *J. Phys. Chem. C*, 2016, **120**, 23989-24001.
- S. Ma, Y. Lan, G. M. J. Perez, S. Moniri and P. J. A. Kenis, *ChemSusChem*, 2014, **7**, 866-874.
- D. Yan, Y. Li, J. Huo, R. Chen, L. Dai and S. Wang, *Adv. Mater.*, 2017, 160408-160416.
- X. Feng, K. Jiang, S. Fan and M. W. Kanan, *J. Am. Chem. Soc.*, 2015, **137**, 4606-4609.
- X. Feng, K. Jiang, S. Fan and M. W. Kanan, *ACS Cent. Sci.*, 2016, **2**, 169-174.
- K. W. Frese, *J. Electrochem. Soc.*, 1991, **138**, 3338-3344.
- Y. Chen, C. W. Li and M. W. Kanan, *J. Am. Chem. Soc.*, 2012, **134**, 19969-19972.
- C. W. Li and M. W. Kanan, *J. Am. Chem. Soc.*, 2012, **134**, 7231-7234.
- Y. Chen and M. W. Kanan, *J. Am. Chem. Soc.*, 2012, **134**, 1986-1989.
- F. Li, S.-F. Zhao, L. Chen, A. Khan, D. R. MacFarlane and J. Zhang, *Energy Environ. Sci.*, 2016, **9**, 216-223.
- F. Li, L. Chen, G. P. Knowles, D. R. MacFarlane and J. Zhang, *Angew. Chem.*, 2017, **56**, 505-509.
- F. Li, L. Chen, M. Xue, T. Williams, Y. Zhang, D. R. MacFarlane and J. Zhang, *Nano Energy*, 2017, **31**, 270-277.
- X. Liu, J. Q. Huang, Q. Zhang and L. Mai, *Adv. Mater.*, 2017, **19**, 1601756-1601759.
- C. Liu, M. P. Lourenço, S. Hedström, F. Cavalca, O. Diaz-Morales, H. A. Duarte, A. Nilsson and L. G. M. Pettersson, *J. Phys. Chem. C*, 2017, **121**, 25010-25017.
- F. Cavalca, R. Ferragut, S. Aghion, A. Eilert, O. Diaz-Morales, C. Liu, A. L. Koh, T. W. Hansen, L. G. M. Pettersson and A. Nilsson, *J. Phys. Chem. C*, 2017, **121**, 25003-25009.
- D. Gao, F. Scholten and B. Roldan Cuenya, *ACS Catal.*, 2017, **7**, 5112-5120.
- Y. Huang, Y. Deng, A. D. Handoko, G. K. L. Goh and B. S. Yeo, *ChemSusChem* 2017, DOI: doi:10.1002/cssc.201701314.
- X. Zheng, P. De Luna, F. P. G. de Arquer, B. Zhang, N. Becknell, M. B. Ross, Y. Li, M. N. Banis, Y. Li and M. Liu, *Joule*, 2017, **1**, 1-12.
- H. Zhong, Y. Qiu, T. Zhang, X. Li, H. Zhang and X. Chen, *J. Mater. Chem. A*, 2016, **4**, 13746-13753.
- P. Su, W. Xu, Y. Qiu, T. Zhang, X. Li and H. Zhang, *ChemSusChem*, 2018, DOI: 10.1002/cssc.201702229.
- J. L. DiMeglio and J. Rosenthal, *J. Am. Chem. Soc.*, 2013, **135**, 8798-8801.
- Z. Zhang, M. Chi, G. M. Veith, P. Zhang, D. A. Lutterman, J. Rosenthal, S. H. Overbury, S. Dai and H. Zhu, *ACS Catal.*, 2016, **6**, 6255-6264.
- L.-L. Long, J.-J. Chen, X. Zhang, A.-Y. Zhang, Y.-X. Huang, Q. Rong and H.-Q. Yu, *NPG Asia Mater.*, 2016, **8**, e263.
- I. A. Ammar and M. W. Khalil, *Electrochim. Acta*, 1971, **16**, 1379-1394.
- D. E. Williams, *Electrochim. Acta*, 1976, **21**, 1097-1098.
- Z. Grubač and M. Metikoš-Huković, *Electrochim. Acta*, 1998, **43**, 3175-3181.
- A. J. Bard, L. R. Faulkner, J. Leddy and C. G. Zoski, *Electrochemical methods: fundamentals and applications*, Wiley New York, 1980.
- J. H. Koh, D. H. Won, T. Eom, N.-K. Kim, K. D. Jung, H. Kim, Y. J. Hwang and B. K. Min, *ACS Catal.*, 2017, **7**, 5071-5077.
- K. Lu, *Materials Science and Engineering: R: Reports*, 1996, **16**, 161-221.
- P. W. Liang, C. Y. Liao, C. C. Chueh, F. Zuo, S. T. Williams, X. K. Xin, J. Lin and A. K. Y. Jen, *Adv. Mater.*, 2014, **26**, 3748-3754.

## Table of content



An urchin-like sulphide-derived bismuth electrocatalyst was synthesised for CO<sub>2</sub> reduction and a maximum of 84.0% faradaic efficiency for formate formation was achieved. The origin of the activity of sulphide-derived bismuth catalyst was explored and the defect-rich structure was responsible for the high formate selectivity.

## Supporting Information

### **Electrochemical reduction of CO<sub>2</sub> on metastable Bi derived from Bi<sub>2</sub>S<sub>3</sub> with enhanced formate selectivity**

Ying Zhang,<sup>a,b</sup> Fengwang Li,<sup>a,b</sup> Xiaolong Zhang,<sup>a</sup> Tim Williams,<sup>c</sup> Christopher D. Easton,<sup>d</sup> Alan. M. Bond<sup>\*a,b</sup> and Jie Zhang<sup>\*a,b</sup>

<sup>a</sup>School of Chemistry, Monash University, Wellington Road, Clayton 3800, VIC, Australia

<sup>b</sup>ARC Centre of Excellence for Electromaterials Science, Monash University, Wellington Road, Clayton 3800, VIC, Australia

<sup>c</sup>Monash Centre for Electron Microscopy, Monash University, Clayton 3800, Victoria, Australia

<sup>d</sup>CSIRO Manufacturing, Bayview Ave, Clayton 3168, Victoria, Australia

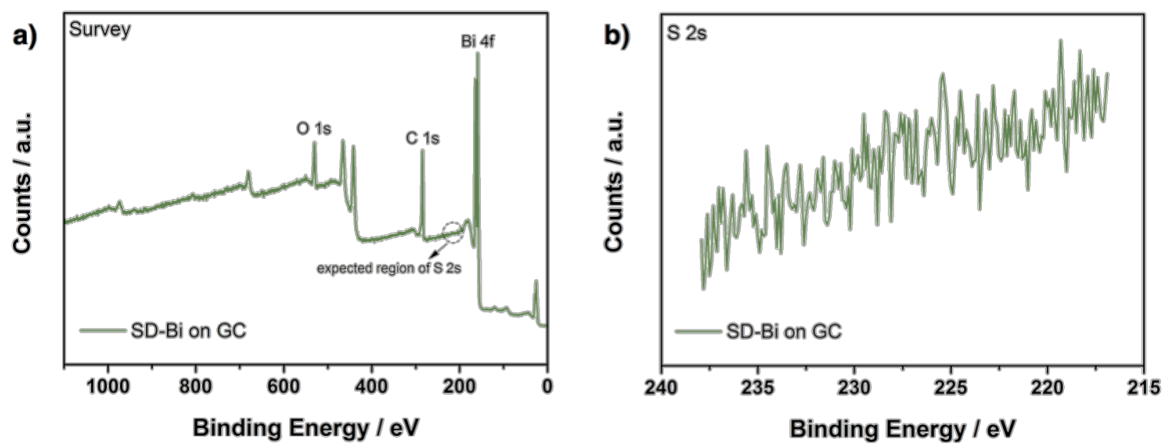


**Figure S1.** The XPS survey spectrum of (a) SD-Bi on GC and (b) the high-resolution scan of S 2s.

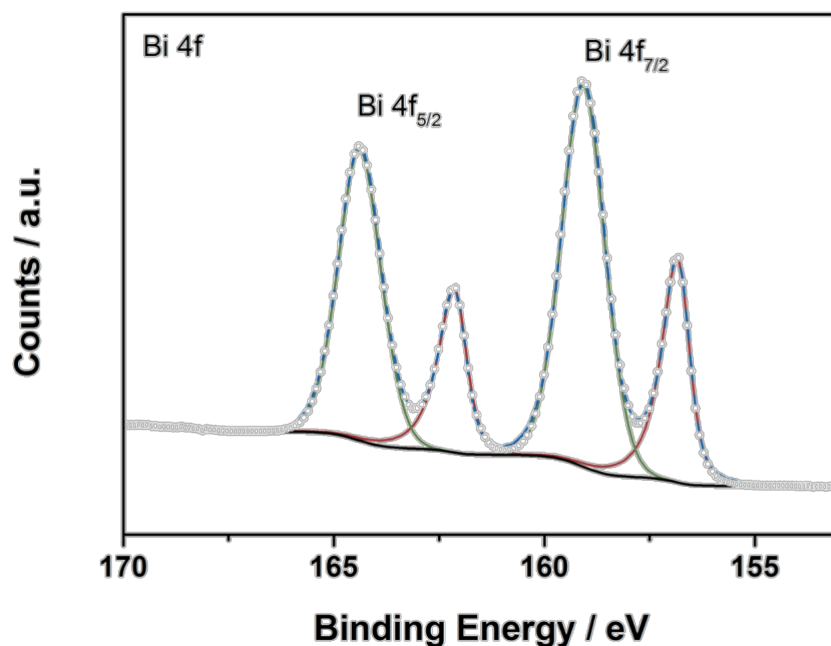
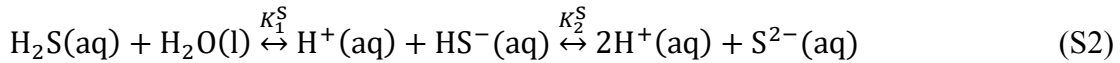
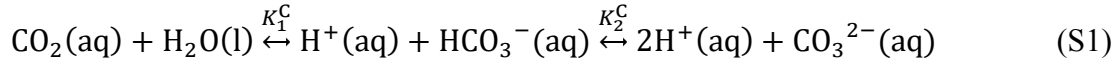


**Figure S2.** High-resolution Bi 4f XPS spectra of SD-Bi on GC. The blue dashed line represents the experimental data and the open circles represent the fitted data. The two red components represent the Bi 4f doublet for Bi(0) with an Lorentzian asymmetric line shape while the two green components represent the Bi 4f doublet for BiO<sub>x</sub> with a Gaussian Lorentzian line shape. The black line represents the Shirley background. The ratio of Bi(0):BiO<sub>x</sub> is roughly 3:7 on the surface of the SD-Bi sample.

Based on the elemental quantification (atomic%) from survey data and fitting of the high resolution Bi 4f spectra, approximately 8.9% of the total 12.7% of Bi is associated with BiO<sub>x</sub>. If the oxide was in the form of Bi<sub>2</sub>O<sub>3</sub> that would result in approximately 13.4% of the total 19.6% of O associated with Bi. The peak shape of the high resolution C 1s spectra is consistent with adventitious carbon including C-O and COOR groups, in addition to a minor contribution from CO<sub>3</sub> groups; fitting this peak indicates that approximately 14.5% of O is associated with C. Accounting for only two contributions to O, Bi<sub>2</sub>O<sub>3</sub> and carbon-oxygen groups, there is insufficient oxygen detected on the surface for the oxide to be in the form Bi<sub>2</sub>O<sub>3</sub> (i.e. 13.4%

$O_{(Bi_2O_3)} + 14.5\% O_{(carbon-oxygen\ groups)} > 19.6\% O_{(total\ measured)}$ ). The origin of oxygen has been discussed below.

When reducing  $Bi_2S_3$  to metallic Bi in a  $CO_2$  saturated 0.5 M aqueous  $NaHCO_3$  solutions, the following equilibria are established.



Where  $K_1^C$ ,  $K_2^C$ ,  $K_1^S$  and  $K_2^S$  are the equilibrium constants and given as

$$K_1^C = \frac{[H^+][HCO_3^-]}{[CO_2(aq)]} \approx \frac{[H^+][HCO_3^-]}{[H_2CO_3^*]} \quad (S3)$$

$$K_2^C = \frac{[H^+][CO_3^{2-}]}{[HCO_3^-]} \quad (S4)$$

$$K_1^S = \frac{[H^+][HS^-]}{[H_2S(aq)]} \quad (S5)$$

$$K_2^S = \frac{[H^+][S^{2-}]}{[HS^-]} \quad (S6)$$

where  $pK_1^C = 6.35$ ,  $pK_2^C = 10.33$ ,  $pK_1^S = 7.05$  and  $pK_2^S = 19$  at 25 °C;  $H_2CO_3^*$  represents  $H_2CO_3$  and dissolved  $CO_2$  in the solution. The total concentrations of dissolved carbon and sulphur species are

$$c_{total}^C = [H_2CO_3^*] + [HCO_3^-] + [CO_3^{2-}] \quad (S7)$$

$$c_{total}^S = [H_2S(aq)] + [HS^-] + [S^{2-}] \quad (S8)$$

Then the concentrations of each species can be derived from the following equations:

$$[CO_3^{2-}] = \frac{K_1^C K_2^C c_{total}^C}{[H^+]^2 + K_1^C [H^+] + K_1^C K_2^C} \quad (S9)$$

$$[HCO_3^-] = \frac{K_1^C [H^+] c_{total}^C}{[H^+]^2 + K_1^C [H^+] + K_1^C K_2^C} \quad (S10)$$

$$[H_2CO_3^*] = c_{total}^C - [CO_3^{2-}] - [HCO_3^-] \quad (S11)$$

$$[S^{2-}] = \frac{K_1^S K_2^S c_{total}^S}{[H^+]^2 + K_1^S [H^+] + K_1^S K_2^S} \quad (S12)$$

$$[\text{HS}^-] = \frac{K_1^S [\text{H}^+] c_{\text{total}}^S}{[\text{H}^+]^2 + K_1^S [\text{H}^+] + K_1^S K_2^S} \quad (\text{S13})$$

$$[\text{H}_2\text{S}] = c_{\text{total}}^S - [\text{S}^{2-}] - [\text{HS}^-] \quad (\text{S14})$$

The concentration of S species is ~0.5 mM if all the Bi<sub>2</sub>S<sub>3</sub> on the working electrode is released into the solution. Thus, the concentration of S<sup>2-</sup> and OH<sup>-</sup> in an electrolyte are calculated to be 4.6×10<sup>-16</sup> mol L<sup>-1</sup> and 1.6×10<sup>-7</sup> mol L<sup>-1</sup> (pH = 7.2), respectively. Therefore, Bi<sub>2</sub>S<sub>3</sub> is thermodynamically more stable upon reduction to metallic Bi than Bi(OH)<sub>3</sub> under our experimental conditions taking into account the difference in their *K<sub>sp</sub>* values (4.0×10<sup>-31</sup> for Bi(OH)<sub>3</sub> vs. 1.8×10<sup>-99</sup> for Bi<sub>2</sub>S<sub>3</sub>). Since Bi<sub>2</sub>S<sub>3</sub> is absent under our experimental conditions with an applied potential of -1.4 V, the presence of BiO<sub>x</sub> is less likely. Therefore, the BiO<sub>x</sub> observed under XPS is most likely from the partial oxidation of Bi by air during sample transfer.

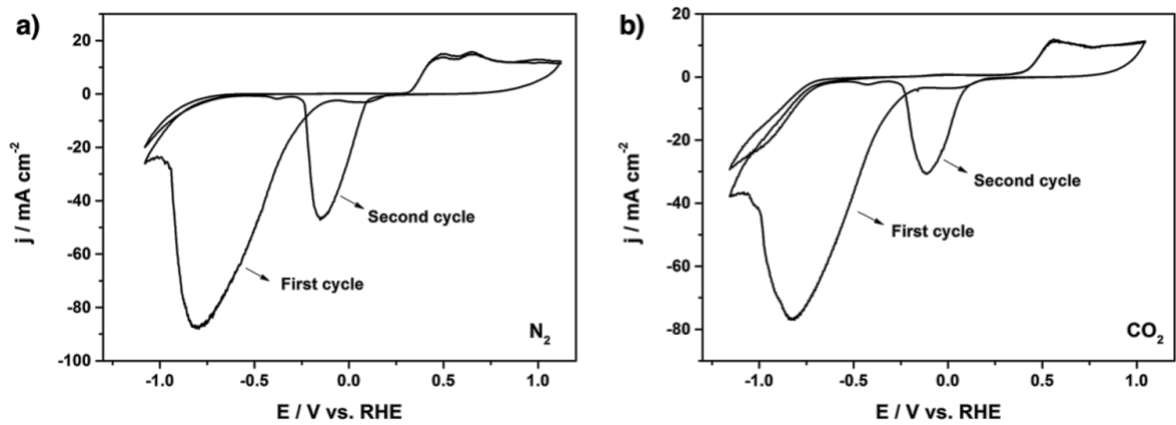


**Figure S3.** The first and second cycle in cyclic voltammograms obtained with  $\text{Bi}_2\text{S}_3$  modified electrode in (a)  $\text{N}_2$  and (b)  $\text{CO}_2$  saturated 0.5 M  $\text{NaHCO}_3$  aqueous electrolyte solution at a scan rate of 50 mV/s under stirring.

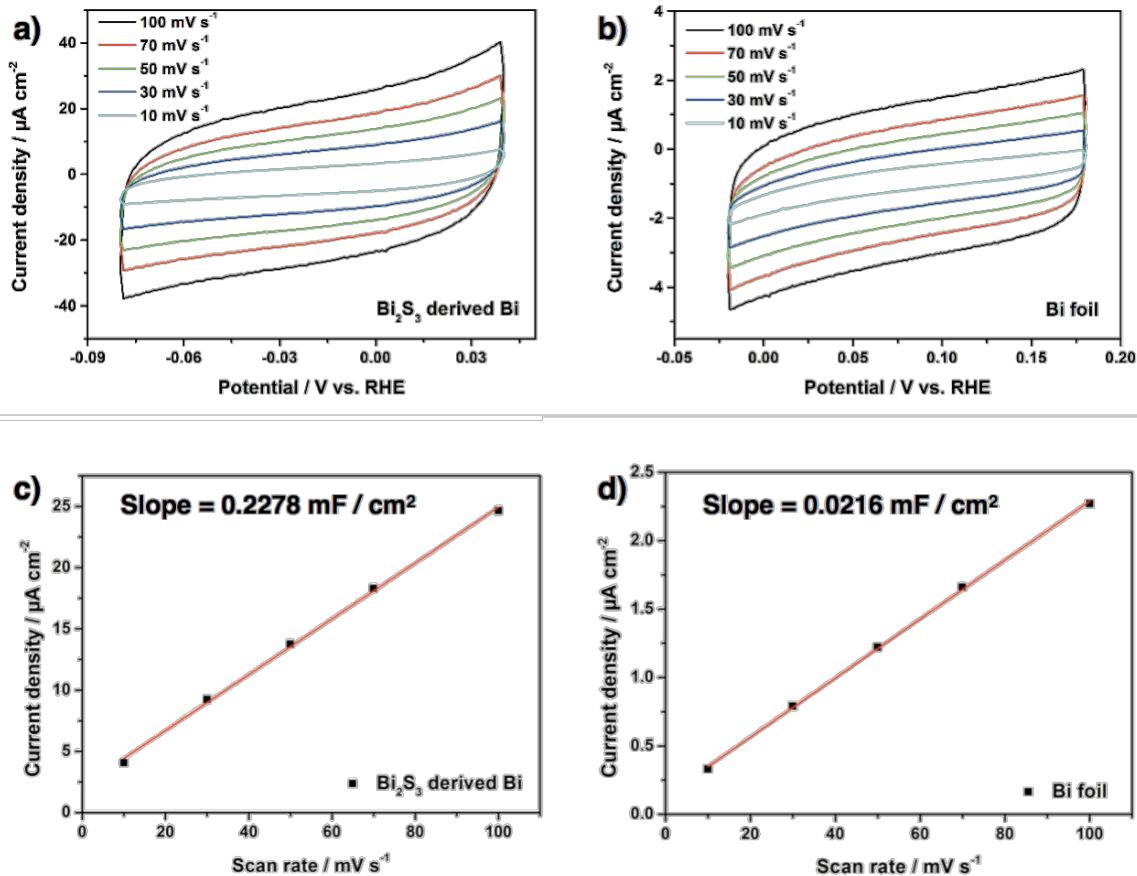


**Figure S4.** Cyclic voltammetric curves of the (a) SD-Bi and (b) Bi foil obtained within a potential range where double-layer charging and discharging are occurring using N<sub>2</sub> saturated 0.5 M NaHCO<sub>3</sub> aqueous solution. The double-layer capacitances of the (c) SD-Bi and (d) Bi foil.

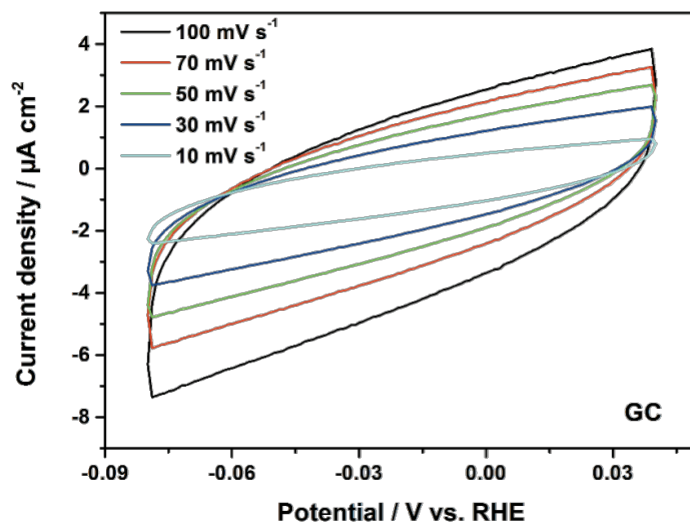


**Figure S5.** Cyclic voltammograms obtained at a GC electrode in  $\text{N}_2$  saturated 0.5 M  $\text{NaHCO}_3$  over a potential range where faradaic current is absent. The double layer capacitance of this GC electrode was determined to be  $0.0252 \text{ mF cm}^{-2}$ .

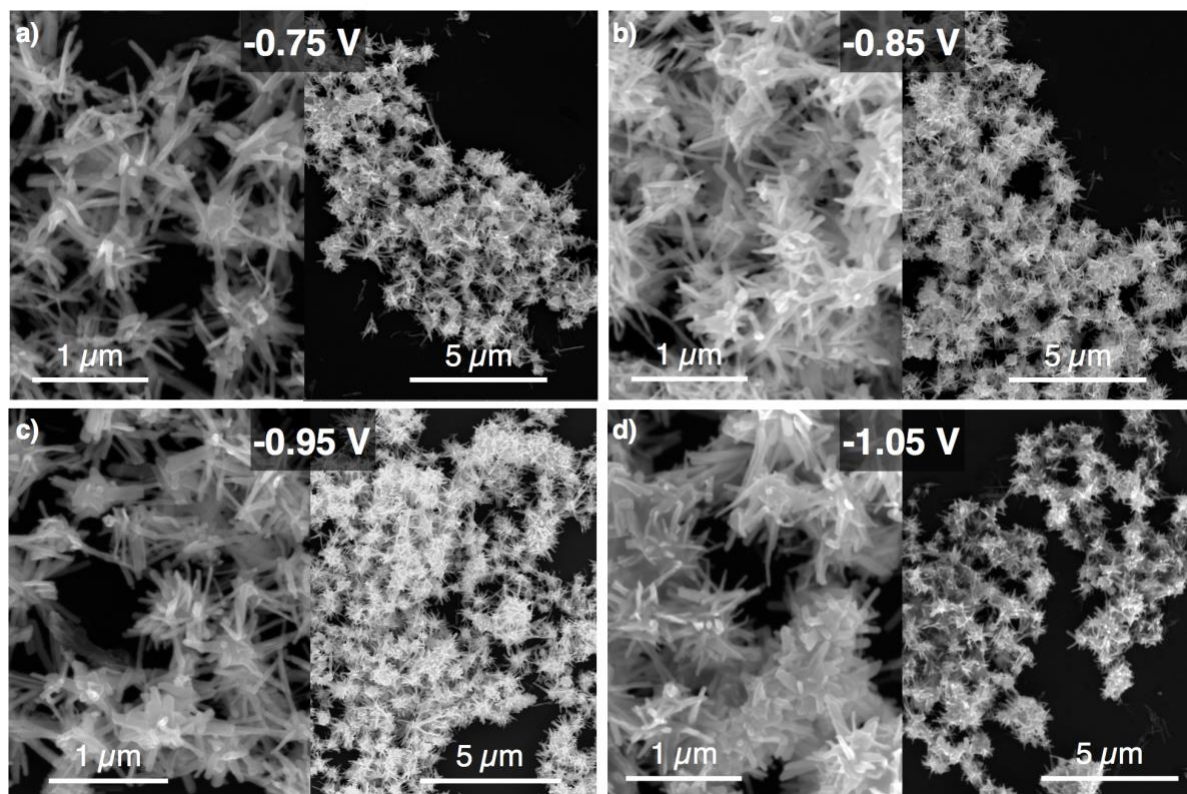


**Figure S6.** SEM images of SD-Bi after 30 min of bulk electrolysis at potentials of -0.75 V, -0.85 V, -0.95 V and -1.05 V with low (right) and high (left) magnification.

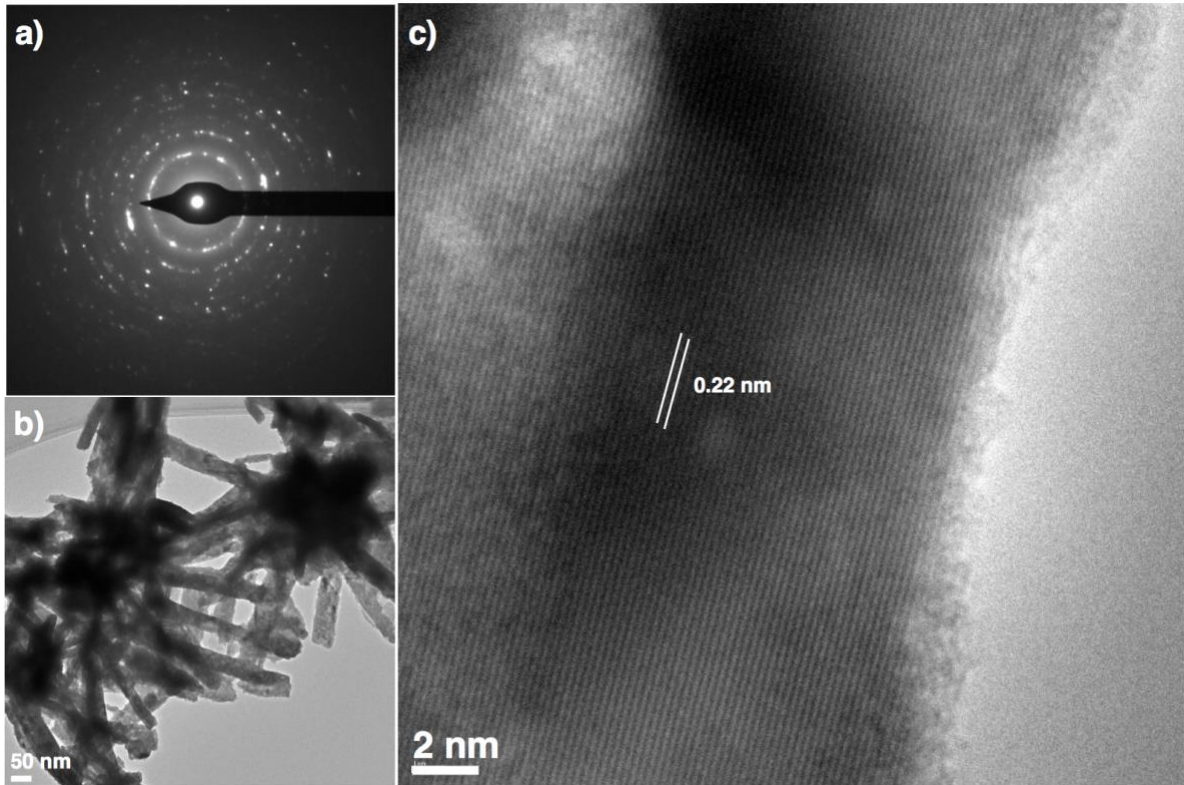


**Figure S7.** (a) SAED pattern, (b) TEM and (c) HRTEM images of SD-Bi post annealing at 150 °C for 30 min. The lattice fringe of 0.22 nm shown in (c) corresponds to the (110) plane of Bi.

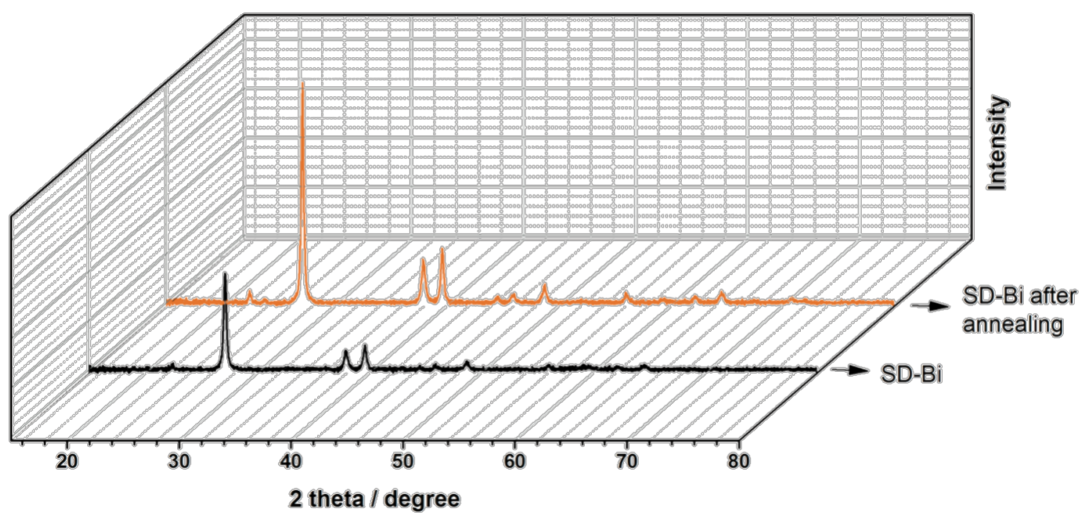


**Figure S8.** XRD patterns of SD-Bi electrode before and post annealing for 30 min at 150 °C.

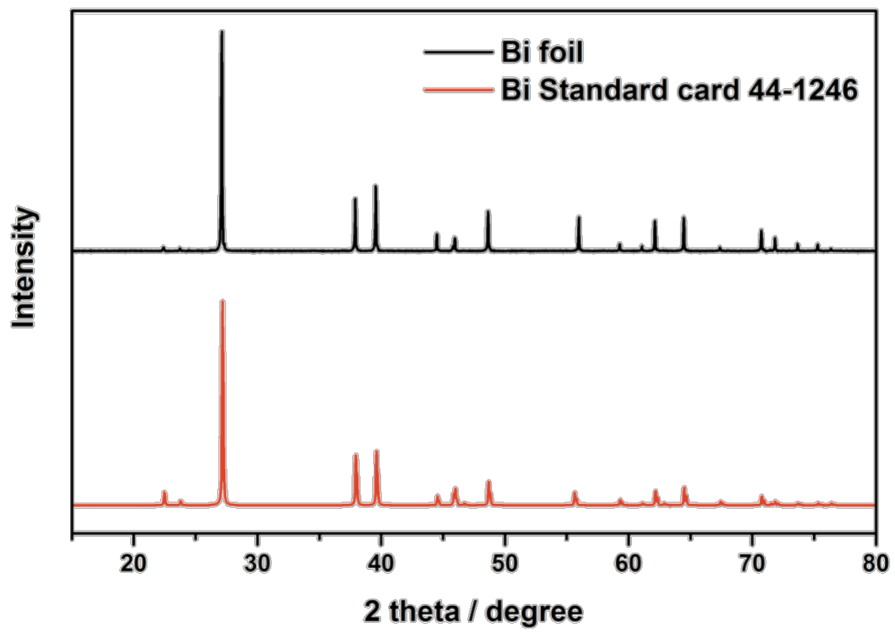


**Figure S9.** XRD patterns of Bi foil and the Bi standard card 44-1246.

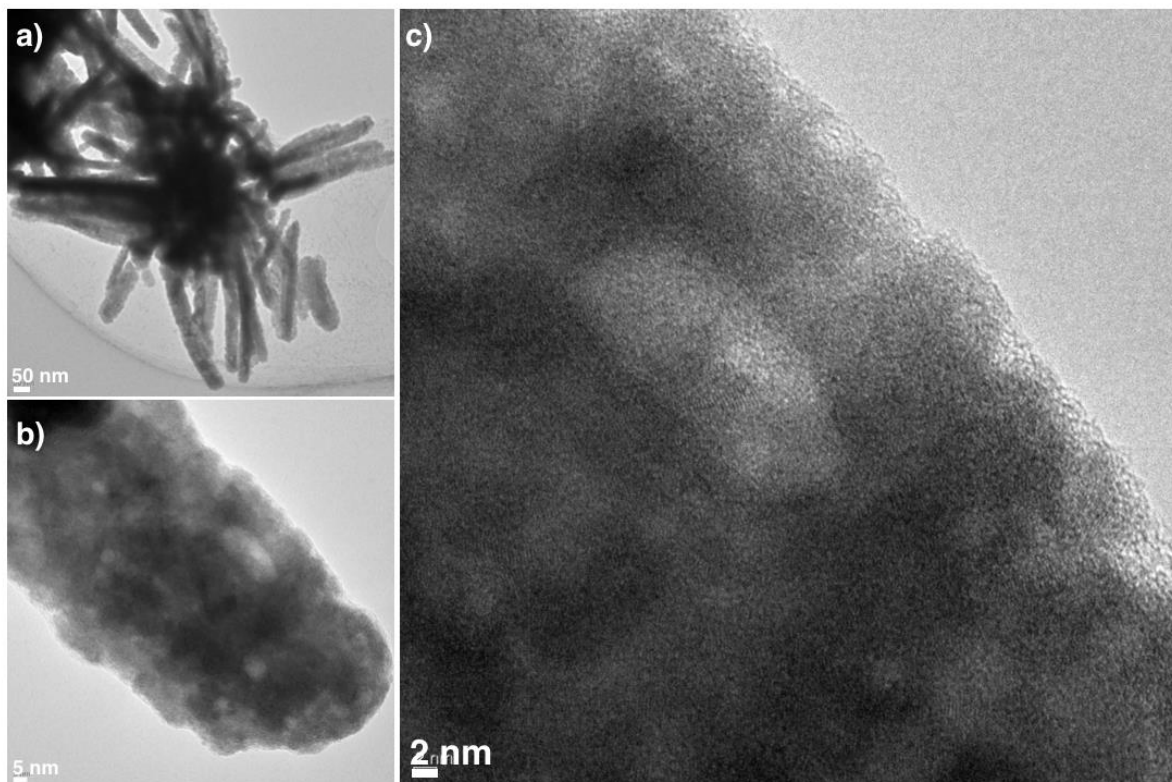


**Figure S10.** (a, b) TEM and (c) HRTEM images of SD-Bi after 24 h bulk electrolysis.

<b>Applied Potential [E / V vs. RHE]</b>		<b>-0.65</b>	<b>-0.75</b>	<b>-0.85</b>	<b>-0.95</b>	<b>-1.05</b>
<b>SD-Bi</b>	FE (formate) [%]	75.0	84.0	82.6	74.5	73.5
	FE (CO) [%]	1.1	1.5	2.6	1.1	1.1
	FE (H <sub>2</sub> ) [%]	29.5	15.6	18.1	31.2	28.6
	Current density [mA cm <sup>-2</sup> ]	-2.40	-6.00	-15.7	-21.1	-27.4
	Partial current density (formate) [mA cm <sup>-2</sup> ]	-1.80	-5.04	-13.0	-15.7	-20.1
	Partial current density (CO) [mA cm <sup>-2</sup> ]	-0.264	-0.0900	-0.408	-0.232	-0.301
	Partial current density (H <sub>2</sub> ) [mA cm <sup>-2</sup> ]	-0.708	-0.936	-2.84	-6.58	-7.84
<b>Bi foil</b>	FE (formate) [%]	36.2	49.5	47.9	32.3	36.4
	FE (CO) [%]	1.4	1.1	1.7	0.8	1.1
	FE (H <sub>2</sub> ) [%]	42.8	56.3	60.2	66.6	50.2
	Current density [mA cm <sup>-2</sup> ]	-1.20	-3.80	-8.10	-13.2	-15.3
	Partial current density (formate) [mA cm <sup>-2</sup> ]	-0.434	-1.90	-3.9	-4.3	-5.6
	Partial current density (CO) [mA cm <sup>-2</sup> ]	-0.0168	-0.0418	-0.138	-0.106	-0.168
	Partial current density (H <sub>2</sub> ) [mA cm <sup>-2</sup> ]	-0.514	-2.14	-4.88	-8.79	-7.68

**Table S1.** Summary of bulk electrolysis data obtained at room temperature for CO<sub>2</sub> reduction with SD-Bi and Bi foil electrodes in a CO<sub>2</sub> saturated 0.5 M NaHCO<sub>3</sub> aqueous electrolyte solution.